Soft Matter

Nanoparticle Diffusion during Gelation of Tetra Poly(ethylene glycol) Provides Insight into Nanoscale Structural Evolution

Journal:	*Soft Matter*
Manuscript ID	SM-ART-11-2019-002192.R1
Article Type:	Paper
Date Submitted by the Author:	03-Jan-2020
Complete List of Authors:	Vaughn, Emmabeth; University of Pennsylvania, Materials Science and Engineering; Bridgestone Americas Holdings Inc Rose, Katie; University of Pennsylvania, Chemical and Biomolecular Engineering Cargnello, Matteo; Stanford University, Department of Chemical Engineering and SUNCAT Center for Interface Science and Catalysis Lee, Daeyeon; University of Pennsylvania, Department of Chemical and Biomolecular Engineering Murray, Christopher; University of Pennsylvania, Materials Science and Engineering; University of Pennsylvania, Chemistry Composto, Russell; University of Pennsylvania, Department of Materials Science and Engineering; University of Pennsylvania, Department of Chemical and Biomolecular Engineering; University of Pennsylvania, Department of Bioengineering

Nanoparticle Diffusion during Gelation of Tetra Poly(ethylene glycol) Provides Insight into Nanoscale Structural Evolution

Emmabeth Parrish,[a] Katie A. Rose,[b] Matteo Cargnello,[c] Christopher B. Murray,[a,d] Daeyeon Lee,[b] Russell J. Composto [a,b,e*]

[a] Department of Materials Science and Engineering, University of Pennsylvania, Philadelphia, PA, USA. E-mail: composto@seas.upenn.edu; Fax: 215-898-8296; Tel: 215-898-4451

[b] Department of Chemical and Biomolecular Engineering, University of Pennsylvania, Philadelphia, PA, USA

[c] Department of Chemical Engineering and SUNCAT Center for Interface Science and Catalysis, Stanford University, Stanford, CA, USA

[d] Department of Chemistry, University of Pennsylvania, Philadelphia, PA, USA

[e] Department of Bioengineering, University of Pennsylvania, Philadelphia, PA, USA

Abstract

Single particle tracking (SPT) of PEG grafted nanoparticles (NPs) was used to examine the gelation of tetra poly(ethylene glycol) (TPEG) succinimidyl glutarate (TPEG-SG) and amine (TPEG-A) terminated stars. As concentration was decreased from 40 to 20 mg/mL, the gel point, t_{gel}, determined from rheometry increased from less than 2 to 44 minutes. NP mobility increased as polymer concentration decreased in the sol state, but remained diffusive at times past the t_{gel} determined from rheometry. Once in the gel state, NP mobility decreased, became sub-diffusive, and eventually localized in all concentrations. The NP displacement distributions were investigated to gain insight into the nanoscale environment. In these relatively homogeneous gels, the onset of sub-diffusivity was marked by a rapid increase in dynamic heterogeneity followed by a decrease consistent with a homogeneous network. We propose a gelation mechanism in which clusters initially form a heterogeneous structure which fills in to form a fully gelled relatively homogenous network. This work aims to examine the kinetics of TPEG gelation and the homogeneity of these novel gels on the nanometer scale, which will aid in the implementation of these gels in biomedical or filtration applications.

1 Introduction

Hydrogels, three-dimensional hydrophilic polymer networks, are used in applications spanning the everyday, such as contact lenses and diapers, to the cutting edge, such as regenerative scaffolds and drug delivery systems. Controlling the structure of the gel is key to achieving consistent properties in these applications. Conventional hydrogels have structural heterogeneity that is intrinsic to their gelation; fluctuations in chain arrangement become immobilized by crosslinking. Since homogeneity in gels is atypical, many researchers have sought to controllably crosslink gels to achieve homogeneous networks.[1–4] Tetra-poly(ethylene glycol) (TPEG) gels are of particular interest because of their tunable arm lengths, high mechanical strength compared to conventional gels,[1,3] and nearly homogeneous structure.[2,5,6] These novel gels were designed by Takai and coworkers[3] and their structure has been studied via small angle neutron scattering (SANS),[5] static light scattering,[6] and dynamic light scattering (DLS).[3] More recently, TPEG gels have been modified to allow for swelling in ionic liquids for use as polymer electrolytes,[4,7–10] to impart self-healing abilities for biomedical usage,[11,12] to act as synthetic sealants for hemostasis,[13] and to control protein and drug release properties.[14–16] Furthermore, due to their homogenous structure, TPEG gels can be systematically altered to introduce heterogeneity by intentionally stopping gelation at a desired conversion rate,[17] using stoichiometrically imbalanced initial conditions,[17,18] or using two different sized TPEG macromonomers.[19] These gels offer a model platform for investigating controlled defect networks and have been used to examine the impact of microscopic hydrogel heterogeneity on mechanical properties and for percolation studies.[17–19] The potential of TPEG gels for use in a variety of biomedical applications has also been highlighted in a recent review article by Shibayama, Li, and Sakai.[20] Applications such as injectable drug delivery systems and selective membranes require precise release and immobilization of nanoscale molecules which depends strongly on the size and heterogeneity of water swollen pores. Thus, understanding how nanoparticles (NPs) diffuse

within TPEG networks and determining how the structure evolves during gelation will aid in the design of these systems.

TPEG gels can be formed by the crosslinking of two disparately terminated four-armed star polymers of equal molecular weight. The chain length between crosslinks is fixed by the arm lengths, which also contributes to the homogeneity in mesh structure.[1] Additionally, the mesh size of TPEGs can be controllably modified by the addition of linear PEG cross-linkers to extend the effective arm length of the TPEG macromonomers.[14,21] The termination chemistries, often amine and activated ester functionalities as used in this study, can only react with each other, not themselves, which largely suppresses heterogeneity. Using infrared (IR) measurements, Akagi and coworkers[22] found that the extent of reaction was close to 0.9 for initial TPEG concentrations in the range of 40 to 140 mg/mL for gels formed from 20 kg/mol TPEG macromonomers, indicating the efficacy of the reaction between end groups. Additionally, proton NMR and Monte Carlo simulations show that the percentage of dangling ends is less than 8% for gels formed at critical overlap concentration (c*), which agrees with the above mentioned IR study.[23] In addition to the macromonomer structure and reaction chemistry, Kurakazu and coworkers[24] found that homogenous mixing, determined largely by the end-group reaction rates, was also important for forming nearly homogenous gels. At high pH, too many amines are un-ionized, resulting in crosslinks forming before macromonomers are fully mixed. At too low pH, activated ester groups hydrolyze before enough amines are un-ionized, preventing crosslinking. Thus, the most homogeneous gels are formed at intermediate pH when mixing is optimal, suggesting a reaction-limited gelation process. Using rheometry to study off stoichiometric mixtures of TPEG macromonomers in the sol or gel state, Sakai and coworkers[25] found that a higher reaction extent was needed to form a gel in dilute solution, which indicates that lattice based gelation models are not applicable in the dilute regime. Additionally, DLS and intrinsic viscosity measurements were used to determine the characteristic scaling relationship of cluster size as the critical gelation point is approached.[26] At low polymer concentrations, the scaling exponent deviates from percolation theory, further

suggesting that lattice based models inadequately describe gelation dynamics for low polymer concentrations and off stoichiometric gels.

It is important to note that while TPEG gels are widely regarded to be microscopically homogenous, topological defects, including double links and other higher order defects, have been identified at the nanoscale for polymer concentrations at and below c*.[23] While not an “ideal” polymer network, the TPEG hydrogel is still one of the most intriguing model networks currently at the disposal of polymer physicists.

Because the mechanism of gelation is suggested to lead to the nearly homogeneous structure, an understanding of the mechanism and kinetics of gelation is important for determining the origin of the final structure. Particle tracking microrheology has been used to study the gelation of a wide variety of network forming polymers.[27–31] Larsen and Furst[27] first used video particle tracking of 1 μm particles to determine the gel time of an amphiphilic β-hairpin peptide, 80 minutes, and the bisacrylamide content needed to form a gel of acrylamide, 0.06 %. Similarly, this technique was used to determine a “gelation map” of varying molecular weights of PEG-heparin hydrogels by identifying a critical logarithmic slope of the mean squared displacement (MSD), 0.45, which separated sol from gel state.[28] Micron scale particles can be used to determine ensemble properties, such as the sol-gel transition and the pore size, of gels with networks smaller than the size of the particle, but are often too large to characterize inhomogeneity in the network. To probe this length scale, nanoprobes must be utilized. Spherical and anisotropic nanoprobes have been previously used to identify and quantify heterogeneity resulting from variations in crosslinking density, or changing local environments during the sol-gel transition, in various hydrogels including poly(acrylamide)[32–34] and poly(*N*-isopropylacrylamide).[35] In TPEG systems, DLS has been used to characterize the ensemble diffusion of nanoparticles, hydrodynamic diameter between 58 nm and 114 nm, during the sol-gel transition for polymer concentrations above c*.[36] Because the final mesh size of the TPEG is on the order of a few nanometers, the diffusion of similarly sized nanoparticles, as investigated here, can provide

new insight into the sol-gel transition for polymer concentrations at and below c*.

While previous studies clarify the chemical reaction mechanism of TPEG gelation and the final structure,[1,6,20] they do not provide information about the spatial homogeneity of the environment during gelation or the impact of polymer concentration on gelation kinetics. In this study, single particle tracking (SPT) of 10 nm diameter PEG grafted NPs was used to examine the gelation of succinimidyl glutarate (TPEG-SG) and amine (TPEG-A) terminated 20kDa TPEG stars, which have average mesh sizes of approximately 3 to 6 nm in the gel state for polymer concentration of 40 to 20 mg/mL.[5] As concentration was decreased from 40 to 20 mg/mL, the time until gelation, t_{gel}, (i.e. sol-gel transition) increased from less than 2 to 44 min, as determined by rheometry. From SPT during gelation, NP mobility and NP spatial coverage increased as polymer concentration decreased in the sol state. Once in the gel state, NP mobility decreased, and NP motion became sub-diffusive and eventually the nanoparticles became localized in all concentrations. We determined the MSD and displacement distributions as a function of increasing time after solutions were mixed, t_{mix}. For all concentrations, the MSD scales as t^1 initially and then decreased to $t^{0.5}$ as gelation time increases. Unexpectedly, the onset of sub-diffusivity was marked by a spike in dynamic heterogeneity, which was attributed to the coexistence of different local environments. This spike in dynamic heterogeneity occurred at longer times as polymer concentration decreased. Experimental results indicate a mechanism in which clusters initially form a heterogeneous structure which fills in over time, resulting in a nearly homogenous network. Ultimately, this work aims to examine the kinetics of TPEG gelation and the homogeneity of these novel gels on the nanometer scale, which will aid in the implementation of these gels in biomedical or filtration applications.

2 Materials and methods

2.1 Materials

Tetra-polyethylene glycol (TPEG) macromeres (20kDa) terminated with succinimidyl glutarate (TPEG-SG) and amine (TPEG-A) functionalities were purchased from Creative PEGWorks.

2.2 Rheometry

Rheometry was performed on a TA Instruments RFS using a 50 mm cone plate geometry. Equal amounts of TPEG-A and TPEG-SG were mixed on the rheometer plate. Data collection began two minutes after mixing ($t = t_{mix} + 2$) due to experimental setup requirements. Oscillatory time testing was performed at 10 rad/s and 1% strain for 2-3 hours.

2.3 Nanoparticle Modification

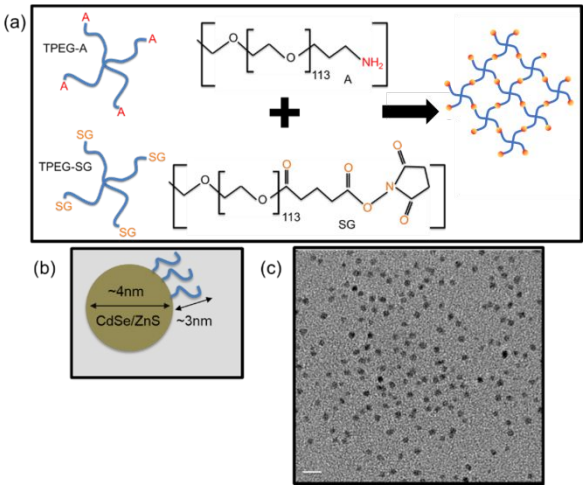

Figure 1: (a) Schematic and chemical structure of TPEG macromers with amine (A) or succinimidyl glutarate (SG) functionalities and the proposed resulting mesh formed in the gel state. (b) The schematic shows quantum dot NP core diameter (4 nm) and PEG brush which combine to yield a 10 nm hydrodynamic diameter. (c) TEM image of NPs, scale bar 20 nm.

Quantum dots (CdSe core/ ZnS shell with 4 nm diameters) with oleic acid ligands on the surface were exchanged with 5 k PEG ligands as follows. Thiol terminated PEG was dissolved in heated toluene (35˚C, 30 mg/ nM). Quantum dots were then added to the toluene and the solution was mixed overnight. Hexane was added to the toluene to aggregate the quantum dots, which were then centrifuged at 8500 rpm for 10 minutes. The supernatant was removed, and the pellet was dried to remove residual organic solvent. Water was then added (10 mL) to resuspend the quantum dots. Centrifugal filters (30 kDa, 6200 rpm, 20 min) were used to remove excess free PEG ligands. The presence of PEG brushes on the surface was confirmed by the particle's dispersion in water and the increased separation between QDs observed in TEM images. The quantum dots' diffusion in a solution of 90 wt% glycerol in water, which had a viscosity of 0.194 Pa s at 22˚C, was used to determine the hydrodynamic diameter, 10 nm, from the Stokes-Einstein relationship.[32] No particle aggregation was observed in these solutions, even at long times. Particle aggregation would lead to changes in particle trajectories as well as the continued visualization of multiple particle aggregates (i.e., versus "blinking" expected for single particles). Dynamic light scattering could not be used to measure particle size as the emission of the particles confounds the detection of scattered light.

2.4 Single Particle Tracking during TPEG gelation

Equal amounts of TPEG-A and TPEG-SG (40, 30, 20 mg/mL) were dissolved in DI water (pH ~ 6), along with 0.4-0.8 nM quantum dots. Just prior to testing, TPEG-A and TPEG-SG were mixed stoichiometrically on a coverslip and another coverslip was placed on top to spread the solution over the coverslip. SPT was performed within seconds of mixing (t = t_{mix}= 0) as described before.[31,32,35] Briefly, SPT experiments were performed on a Nikon Eclipse Ti with an inverted optical microscope (×100, 1.49 NA objective) using a 532 nm laser to excite the quantum dots. A frame rate of 25 fps was used to collect videos every 1 to 5 minutes until NPs had been visually localized for 10 minutes. FIESTA (Fluorescence Image Evaluation Software for Tracking and Analysis)[37] was used to determine particle trajectories. Two minutes of video were used to collect between 60 and 100 particle trajectories per time point since mixing. The MSD of each NP was determined using the MATLAB program, msdanalyzer.[38] The MSD is the expectation value for the distance traveled in a given amount of time as shown below, where $\boldsymbol{\tau_i}$ is the time between positions, r, being compared.

$$\boldsymbol{MSD}(\boldsymbol{\tau}) = \ <\boldsymbol{\Delta r}(\boldsymbol{\tau})^2> \ = \ <[\boldsymbol{r}(\boldsymbol{\tau}+\boldsymbol{\tau_i}) - \ \boldsymbol{r}(\boldsymbol{\tau})]^2> \quad (1)$$

To evaluate the time dependence of the MSD, Equation 2 was used, where α is the slope of the MSD versus time graph plotted on a log-log scale.

$$\boldsymbol{MSD} = \boldsymbol{D\tau^{\alpha}} \quad (2)$$

An in-house MATLAB code was used to determine displacement distribution and non-Gaussian parameters, as described previously.[31,32] Briefly, displacement distributions were determined by[39]

$$\Delta \boldsymbol{x} \ = \ \boldsymbol{x}(\boldsymbol{\tau} \ + \boldsymbol{\tau_i}) - \boldsymbol{x}(\boldsymbol{\tau}) \quad (3)$$

where τ_i is a specific time interval between positions and x can be changed with y to obtain displacements along both the x and y axis. The non-Gaussian parameter, N_g, compares the second and fourth moments of the displacement distributions as follows[40]

$$\boldsymbol{N_g} = \frac{\langle \boldsymbol{\Delta x^4} \rangle}{3\langle \boldsymbol{\Delta x^2} \rangle^2} - \mathbf{1}. \quad (4)$$

3 Results and Discussion

TPEG star polymers were studied using rheometry and SPT of PEG functionalized NPs to determine how the structure evolved and how NPs diffused within TPEG networks during gelation. The 20kDa precursor macromonomers, TPEG-A and TPEG-SG, shown in Figure 1a, were terminated with either amine (A) or succinimidyl glutarate (SG) functionalities, prohibiting self-crosslinking. The macromonomers were mixed in DI water (pH ~ 6) at stochiometric ratios to form gels via an aminolysis reaction.[1] Three concentrations were used, 40, 30, and 20 mg/mL, to understand the impact of concentration on gelation kinetics and the resulting nanoenvironments. Rheometry was used to identify the onset of network formation, t_{gel}. SPT was performed using quantum dot NPs grafted with 5kDa PEG brushes, Figure 1b, which were added to the TPEG solution prior to mixing. NP trajectories during gelation were analyzed by their spatial coverage, MSD, time dependence of the MSD, and displacement distribution. As expected, increasing initial TPEG concentration decreased t_{gel}, as well as NP mobility and spatial coverage in the sol state. However, after t_{gel}, NPs become localized within the gel and exhibit non-Gaussian dynamics at intermediate times.

3.1 Rheometry of TPEG hydrogel during gelation

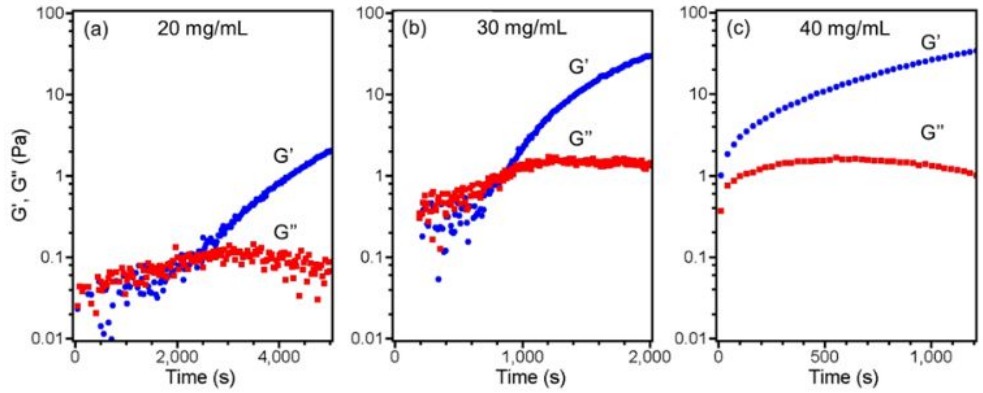

Figure 2: Temporal evolution of the storage, G' (blue), and loss, G'' (red), moduli from oscillatory cone plate rheometry (10 rad/s and 1% strain) for (a) 20 mg/mL, (b) 30 mg/mL, and (c) 40 mg/mL TPEG samples. The crossover of G' and G'' denotes the gel point, t_{gel}. Data comes from one sample but is representative of at least two separate measurements.

Oscillatory rheometry (10 rad/s, 1% strain) experiments were performed for three TPEG concentrations, 20, 30, and 40 mg/mL, to determine the time for the formation of an elastically deformable network, t_{gel}. According to the Winter-Chambon criterion, the gel point of a system occurs when G' and G'' display the same power-law frequency dependence.[41] In this study, we simply use the crossover of G' and G'', signifying a phase transition from liquid-like to solid-like behavior, as an indication of network formation observed by oscillatory rheometry. It is this time point that is compared to the transition time observed by SPT . Figure 2 shows the time dependence of the storage, G', and loss, G'', moduli as a function of increasing TPEG concentration. Measurements began two minutes after TPEG-A and TPEG-SG were mixed (t = 2 min) to allow for experimental setup. For the 20 mg/ml sample, Figure 2a, G' was initially smaller than G''. A crossover occurred at 0.1 Pa, 44 minutes after t_{mix}, when G' became larger than G'', and then rapidly increased. This transition was taken as t_{gel}. The 30 mg/ml sample also initially had a smaller G' than G'', Figure 2b. However, G' became larger than G'' after only 17 minutes after t_{mix} at a modulus value of 0.9 Pa.

At the highest concentration, 40 mg/ml, G' is always larger than G'', Figure 2c, and thus t_{gel} for this system was taken to be less than 2 min. For all concentrations, G' increased with increasing t. The value of G' at t = 2 minutes increased by two orders of magnitude, from 0.02 to 1 Pa as the concentration

increased from 20 to 40 mg/mL. Rheometry experiments on TPEG systems with various terminal groups report moduli in the range of 0.1 to 1 Pa for the sol state at 1% strain at a frequencies between 6.28 and 10 rad/sec, in good agreement with our results.[12,42] Additionally, for hydroxyl end-functionalized TPEG polymers, the storage and loss moduli crossover was observed between 0.1 to 1 Pa for pH values between 4.5 and 12.5, over times ranging from 0 to 2,000 s, similar to the crossover times observed in this study.[12]

3.2 SPT and MSD of TPEG polymer during gelation

After identifying the t_{gel} with rheometry, SPT was performed using 10 nm quantum dot NPs functionalized with 5kDa PEG brushes. Figure 3 shows the evolution of the NP trajectories with t for TPEG concentrations of 40 mg/mL (red box), 30 mg/mL (blue box), and 20 mg/mL (orange box). Video collection began within seconds of mixing TPEG-A and TPEG-SG, t = 0. All trajectories were initialized at the (x,y) position (0,0) so that trends in overall spatial coverage could be observed. For the 40 mg/mL samples, t = 10, 20, and 25 minutes show the decreasing trajectory lengths with increasing time since t_{mix}. Similarly, the NP trajectories are additionally shown at t = 40 and 40, 90, and 105 minutes for the 30 and 20 mg/mL samples, respectively, to display the complete evolution of NP trajectories as t increased. At t = 10 minutes, some NPs were able to cover distances greater than 2.5 μm at all concentrations. As time after t_{mix} increased, the spatial coverage of the NPs decreased in all concentrations. In the 40 mg/mL sample, most NPs traveled less than 1 μm at 20 min, whereas this limitation in trajectory length was not observed until longer times as concentration decreased, namely t = 25 and 70 minutes for 30 and 20 mg/mL, respectively. At long enough times, NPs became localized in all concentrations. NPs were categorized as localized when the spatial coverage was less than 500 nm and the spatial coverage did not change for 10 minutes. As polymer concentration decreased, the time after t_{mix} until localization of the NPs increased. Specifically, NPs became localized near t = 25 min, 40 min, and 105 min in the 40, 30, and 20 mg/mL samples, respectively. For all concentrations, these times are greater than twice t_{gel} determined from rheometry, namely 2, 17, and 44 minutes, respectively. Interestingly, some NPs were able to move

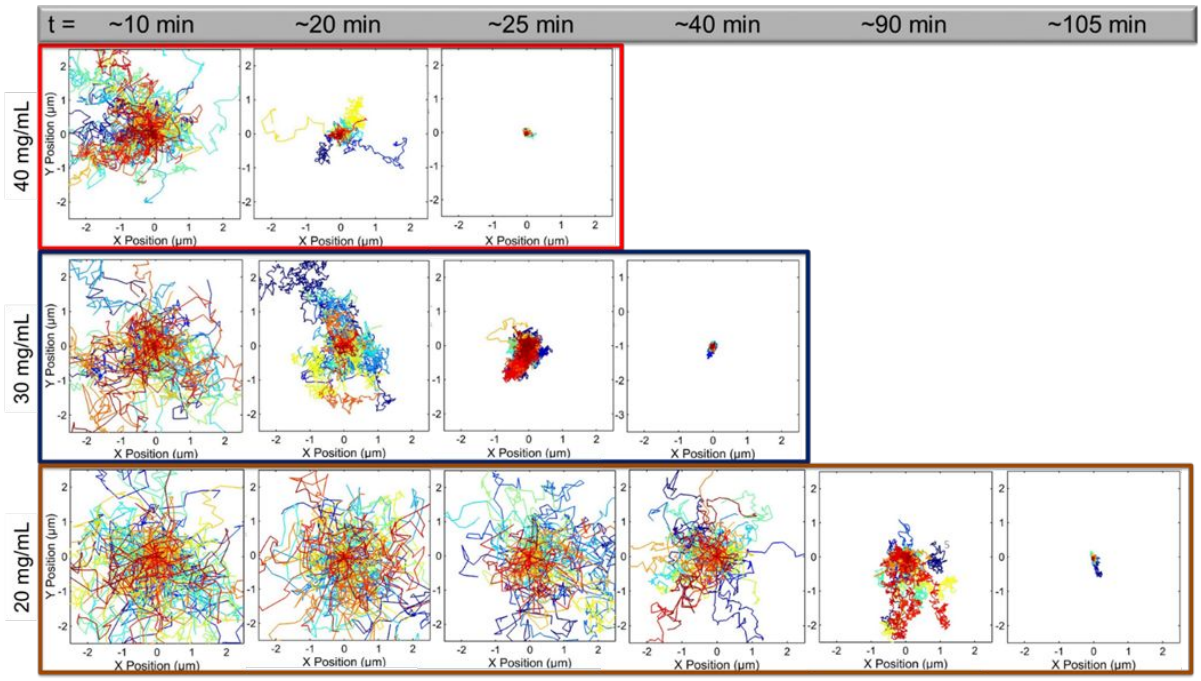

Figure 3: SPT NP trajectories in 40mg/mL (top red box), 30 mg/mL (middle blue box), and 20 mg/mL (bottom orange box) TPEG samples plotted in XY space (-2.5μm x 2.5μm). The time since t_{mix} is listed across the top in the grey box. Different colors represent different individual trajectories.

distances greater than 2.5 μm at times longer than t_{gel} determined from rheometry. This likely indicates that the initial network formed was relatively open, with mesh sizes larger than the hydrodynamic diameter of the NPs, 10 nm.

MSD curves give the average squared displacement of the NPs from their initial positions as a function of time, $\boldsymbol{\tau}$. By comparing MSD plots, the evolution of the spatial coverage of NPs with time since t_{mix} can be quantified. This study involves two-time increments, the gelation time, t, which is measured in minutes, and the diffusion time of the NPs, $\boldsymbol{\tau}$, which is measured in seconds. The ensemble averaged MSD (mean MSD) at a series of times after t_{mix} for each concentration are shown in Figure 4a-c. In each graph of Figure 4a-c, the magnitude of the mean MSD curves decreased with increasing time since t_{mix}, light blue curves to red curves. Additionally, for all concentrations, the slope of the mean MSD line also decreased with increasing time since t_{mix}. As shown in Equation 2, the time dependence of the MSD is designated by α, which is given by the slope in the log-log plots of Figure 4. For the 20 mg/mL sample, Figure

4a, the slope of the mean MSD at t = 10 minutes (light blue) is 1, consistent with random diffusive motion of the NPs; at t = 105 minutes, the slope decreased to 0.58, indicating confined motion of the NPs. Similarly, at t = 10 minutes, the MSD curves of the 30 and 40 mg/mL samples had slopes of approximately 1, while at the longest times shown, 40 and 25 minutes, the slopes were 0.4 and 0.2 for the 30 and 40 mg/mL samples, respectively.

Microrheological measurements of the sol-gel transition have used changes in the slope of the MSD, α, to identify the onset of network formation. Thus, the change in α determined from MSD curves can be used to denote the transition time separating liquid-like to solid-like behavior as α changes from $\alpha \approx 1$ to $\alpha < 1$.[27,28] In our system at all concentrations, the transition to α values less than 0.6 occurs after the onset of network formation determined from rheometry. This value is in reasonable agreement with what is seen in the literature for single gelling systems, where critical α values range from 0.45 to 0.6.[27–30] Thus, even during network formation, NPs were able to move diffusively and the network does not cause sub-diffusive behavior of the NPs until after the near completion of network formation.

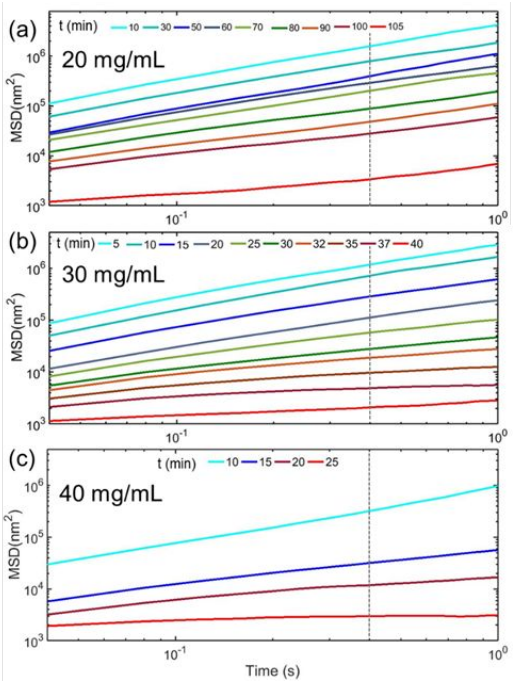

Figure 4: Mean MSD curves with increasing time since mixing of (a) 20 mg/mL, (b) 30 mg/mL, and (c) 40 mg/mL TPEG. Color denotes early (sol) and late (gel) times from blue to red, respectively. Slopes decrease with increasing time. Both x and y axes are the same scale in all three graphs. Light grey dashed line indicates τ = 0.4 s. MSD values from all NP trajectories at τ = 0.4 s are evaluated in Figure 5.

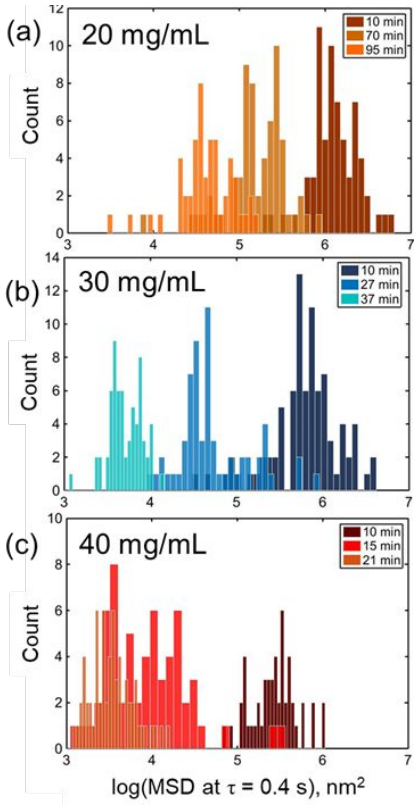

Figure 5: Histogram of individual particle MSDs at τ = 0.4 s for (a) 20 mg/mL TPEG at t = 10, 70, and 95 minutes, (b) 30 mg/mL TPEG at t = 10, 27, and 37 minutes, and (c) 40 mg/mL TPEG at t = 10, 15, and 21 minutes. X axis is the same scale for a-c.

Because gelation is a dynamic process, NPs may explore different local environments as the system evolves. Whereas Figure 4 represents the ensemble average mobility, quantifying the behavior of individual NPs allows for the presence of different environments to be identified and provides further insight into the nature of the environment sampled by NPs. For each concentration, Figure 5 shows the distribution of MSDs at $\boldsymbol{\tau}$ = 0.4 s (dotted line in Fig. 4) for three times since t_{mix} to display the full range of NP behavior. The times were chosen as follows: a time shortly after t_{mix} (t =10 minutes), a time past the rheometric t_{gel} (t = 70, 27, 15 minutes for 20, 30, and 40 mg/mL samples, respectively), and a time just before NP localization as determined from SPT, Figure 3, (t = 95, 37, 21 minutes for 20, 30, and 40 mg/mL samples, respectively). For the 20 mg/mL sample, the average values of the MSD distributions decreased by almost an order of magnitude at t = 10 and 70 minutes from 10^6 nm^2 (1000^2 nm^2) to $10^{5.2}$ nm^2 (398^2 nm^2), respectively, and then again from 70 to 95 minutes to a value of $10^{4.6}$ nm^2 (200^2 nm^2). Despite the 60-minute time difference between 10 and 70 minutes, which correspond to times before and after the rheometric t_{gel}, some MSD values overlap. Additionally, MSD values overlap between the t = 70-min. and 95-min. populations. In the 30 mg/mL sample, from t = 10 to 37 minutes, the distribution center decreased from $10^{5.7}$ nm^2 (708^2 nm^2) to $10^{3.7}$ nm^2 (71^2 nm^2). Like the 20 mg/mL sample, at the middle time point, t = 27 minutes, which corresponds to 10 minutes after the rheometric t_{gel}, the MSD values overlap with both the shorter and longer time populations. In the 40 mg/mL sample, from t = 10 to 21 minutes, the distribution centers decreased from $10^{5.6}$ nm^2 (631^2 nm^2) to $10^{3.5}$ nm^2 (56^2 nm^2). At the intermediate time, t = 15 min, the distribution extends from 10^3 (32^2 nm^2) to $10^{5.5}$ nm^2 (562^2 nm^2). For each sample concentration at the intermediate times shown in Figure 5, NP mobility ranges multiple orders of magnitude, corresponding to mobilities characteristic of both NPs within the pre-gel sol state, and in the developed network, near localization. This likely indicates that the environment the NPs sampled varied greatly at this intermediate time consistent with maximum network heterogeneity.

Furthermore, for all concentrations, the average MSD shifts toward lower values as gelation proceeds.

3.3 NP displacement distributions in TPEG polymer during gelation

To gain further insight into the origin of the variations in MSD values

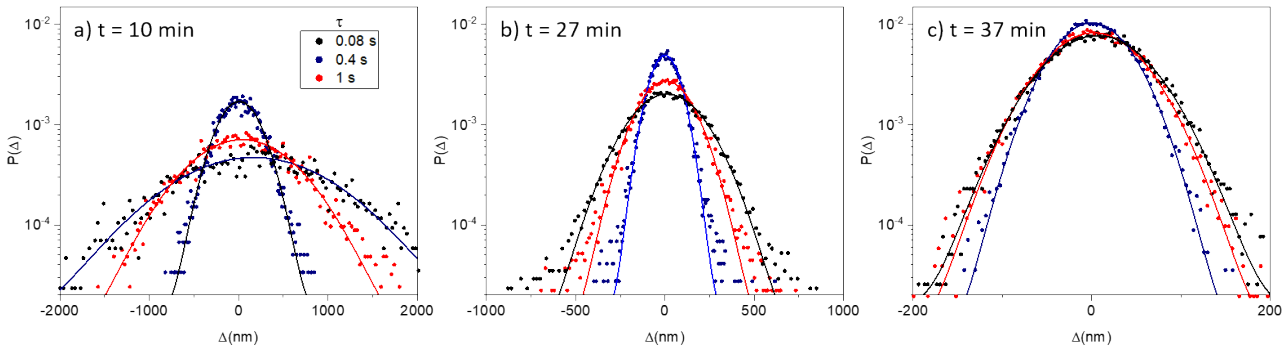

Figure 6: Displacement distributions of 30 mg/mL TPEG sample at t = (a) 10, (b) 27, and (c) 37 minutes measured at τ = 0.08 (blue), 0.4 (red), and 1 (black) s. To aid visualization of data, the x-axis values decrease from ± 2000 to ± 200 nm from (a) to (c). Y-axis values are the same from (a) to (c). The solid lines are fits to a Gaussian distribution. Fitted parameter values are provided in the supplemental material.

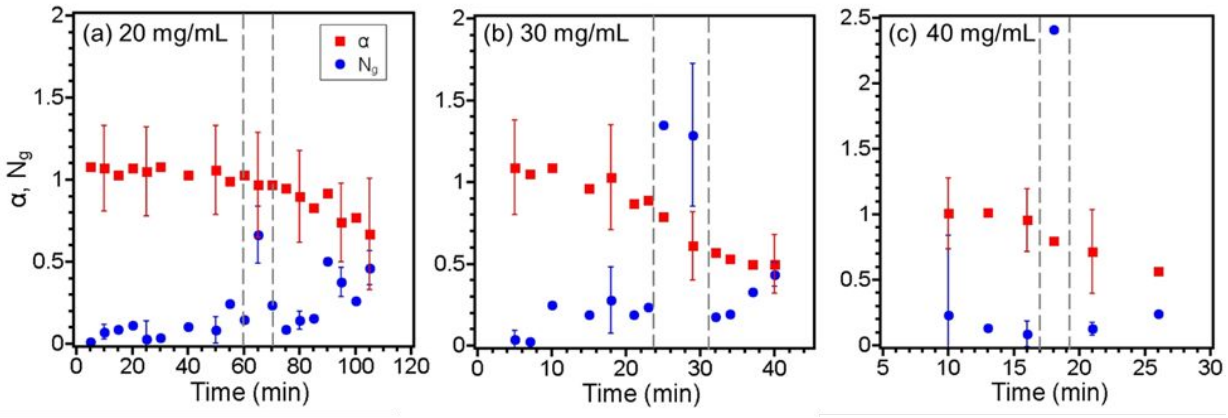

Figure 7: Non-Gaussian, Ng, and α parameters as a function of time since mixing for (a) 20, (b) 30, (c) 40 mg/mL TPEG samples. Representative error bars for Ng come from the standard deviation from the average of values between τ = 0.04 and 1 s. Error bars for α come from the standard deviation. Grey dashes outline time period of spike in Ng.

observed in Figure 5, displacement distributions were calculated as described in Equation 3. The displacement distributions describe the probability that a particle moves a distance along one direction within a specific time interval, $\boldsymbol{\tau_i}$, and are a robust measure of the variation in local environment. Specifically, the distributions allow for the structural nanoheterogeneities on the length scale of the NP size to be measured. In a spatially homogeneous media, displacement distributions will exhibit Gaussian functionality. However, if different local environments exist within the media, the displacement distributions will deviate from a Gaussian function. At each concentration, displacement distributions were determined for $\boldsymbol{\tau}$ = 0.04 to 1 s at a time interval of 0.04 s from t = 0 s until localization of the NPs, 105, 40, and 26 min. for 20, 30, and 40 mg/mL samples, respectively (not shown). Figure 6 shows displacement distributions at $\boldsymbol{\tau}$ = 0.08, 0.4, and 1 s for NPs in a 30 mg/mL sample at t = 10, 27, and 37 minutes, the same times used in the MSD analysis (Figure 5b), as well as fitted Gaussian curves (solid lines). At t = 10 minutes, the displacements exhibited a Gaussian distribution which broadened as $\boldsymbol{\tau}$ increased from 0.08 (blue) to 1 (black) s, with the full width at half maximum (FWHM) of the fitted Gaussian increasing from approximately 500 nm to 2000 nm. At t = 27 minutes, the displacement distributions also broaden with increased time. However, the distributions exhibited a wider tail than would be expected from a Gaussian distribution. To further visualize this difference, quartile-quartile plots comparing the normal

Gaussian distribution to the displacement distributions are available in the supplemental material (see SI). At t = 37 minutes, the displacements showed little time dependence, with the FWHM increasing from 90 nm for τ = 0.08s to only 120 nm for τ = 1s. However, the displacements returned to a Gaussian distribution consistent with a more homogeneous network. The non-Gaussian behavior at intermediate times, i.e. t = 27 minutes, is consistent with heterogeneous local environments probed by the 10 nm NPs, likely due to variations in mesh size.

The non-Gaussian parameter, N_g, determined from Equation 4 can be used to quantify the deviation from Gaussian behavior.[40] N_g is a comparison of the breadth of the distribution to its variance and describes the extent of heterogeneity in dynamics within the ensemble. An N_g value of 0 represents Gaussian behavior, whereas higher values of N_g represent greater deviations from Gaussian behavior. Figure 7 shows the N_g values, plotted in blue, as a function of time since t_{mix} for each concentration. The representative error bars shown were determined from the standard deviation of the N_g values between τ = 0.04 and 1 s. Also shown in Figure 7 are the average α values, plotted in red, for each time, t, since t_{mix}. The average α values were determined from fitting the slope of the MSD for all trajectories to determine the average time dependence. The representative error bars are the standard deviation from the average. For the 20 mg/mL sample, Figure 7a, the α value remained approximately 1 from t = 5 to 65 minutes, then monotonically decreased between t = 65 and 105 minutes to a value of 0.6. Correspondingly, the N_g values of the displacement distributions increased gradually as t increased from 5 to 60 minutes, from a N_g value of 0.02 to 0.15. At t = 65 minutes, N_g spiked to 0.7, before returning to 0.24 at 70 minutes. From t = 75 to 105 minutes, the N_g value increased from 0.1 to 0.46, as the NPs became localized based on the spatial coverage, Figure 3. In Figure 7b, the 30 mg/mL sample, the α value remained approximately 1 from t = 5 to 20 minutes, then decreased from t = 23 to 40 minutes to a value of 0.5. Again, the N_g values increased slightly with increasing time, but were less than 0.5, except from t = 25 to 29 minutes when the value increased to 1.3. As the NPs reached localization, the N_g value

Table 1: Summary of characteristic time points during the gelation of TPEG samples at concentrations of 20, 30, and 40 mg/mL.

approached 0.4. In Figure 7c, the α value was approximately 1 from t = 10 to 15 minutes, then decreased to 0.57 at 26 minutes. In this sample, a spike in N_g was observed at t = 19 minutes to a value of 2.2, whereas at all other times, the N_g value was less than 0.3. When the NPs were localized, the N_g value was approximately 0.24. These experiments were repeated on different days and similar values of N_g and α were determined. For example, in the repeated 40 mg/mL sample the N_g value jumped from 0.7 to 1.2 at t = 14 and 16 minutes, respectively, then dropped to 0.22 at 20 minutes (see SI).

Two common trends are present in Figure 7 for each concentration, a change in α from diffusive to sub-diffusive behavior, and non-monotonic behavior in N_g. Initially after mixing, NPs moved diffusively at all concentrations. As time increased, NP motion transitioned to sub-diffusive behavior, with the transition occurring at longer times with decreasing concentration. The α value decreased to less than 1 at t = 16, 23, and 65 minutes for 40, 30, and 20 mg/mL samples, respectively. This decrease occurred at times longer than the rheological t_{gel}. For each concentration, Table 1 lists t_{gel} determined from rheometry, as well as key time points identified from SPT. With increasing concentration, the spike in N_g also occurred at increasing times. The spike occurred almost concurrent with the onset of sub-diffusive behavior, at t = 19, 25, and 65 minutes for 40, 30, and 20 mg/mL samples, respectively.

[i] **from rheology** Figure 2 [ii] **from SPT** Figure 7 [iii] **from SPT** Figure 3

Concentration (mg/mL)	Gel Point [i] (min)	Onset of Subdiffusivity [ii] (min)	Time at Highest N_g [ii] (min)	Time of Localization [iii] (min)
20	44	65	65	105
30	17	23	25	40
40	≤ 2	16	19	26

Additionally, the final value of N_g decreased with increasing concentration, 0.46, 0.4, and 0.24 for 20, 30, and 40 mg/mL, respectively. The high homogeneity of the final network of the 40 mg/mL sample is in agreement with SANS studies which found 40 mg/mL to be the overlap concentration for 20k TPEG stars.[5] The increased final N_g value, increased dynamic heterogeneity, as concentration was decreased from 40 mg/mL to 20 mg/mL likely corresponds to the increased presence of missing crosslinks within the network at concentrations lower than the overlap concentration.

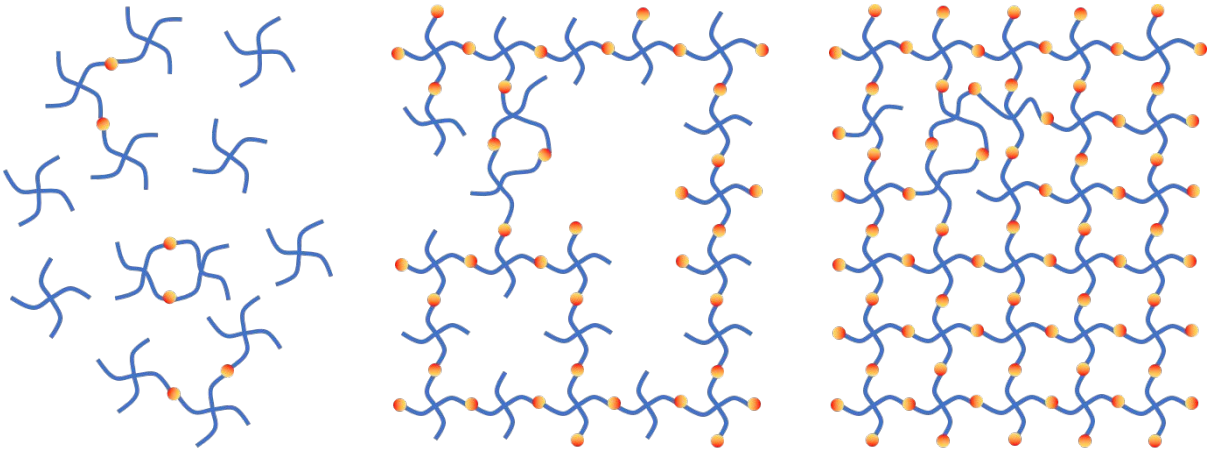

Figure 8: 2-D Schematic of TPEG gelation mechanism. (a) Open network where NPs mobility is mainly through the sol. (b) Network with heterogeneity in the mesh resulting in NPs exhibiting dynamic heterogeneity as reflected by high N_g. (c) Relatively homogeneous network that localizes NPs. The presence of some topological defects, such as a double loop and dangling ends, are expected in these networks. Network shown corresponds to 40 mg/mL samples; the network corresponding to 20 and 30 mg/mL samples will exhibit similar behavior, however fewer crosslinks will form resulting in more defects.

The physical meaning of the changes in the N_g can be explained by the changes and variations in the local environment during gelation. Just after mixing, the NPs explored a homogeneous environment, moving diffusively through the sol or very open network, indicated by the α parameter of 1 and the low N_g. Even after the t_{gel}, the NPs were able to move diffusively. This suggests that the initial network had a mesh structure much larger than the diameter of the NPs, 10 nm. As time increased, the NPs began to sample different local environments due to heterogeneity in the network structure, which differentially hindered NP diffusion. As the gel continued to form, the network reached a peak in heterogeneity (i.e., distribution of pore sizes). This condition corresponded to the onset of subdiffusivity and peak in N_g as shown in Figure 7. After this peak, the network filled in, becoming more homogeneous, and further inhibiting the motion of the NPs. The localization of the NPs due to the network was indicated by the subdiffusive behavior, α ≈ 0.5, which is characteristic of localization, or caged mobility. The final network became more homogeneous (i.e., uniform in pore size) as the concentration of TPEG increased, consistent with the lower final values of N_g. The gelation process is shown schematically in Figure 8. Simulations of TPEG gelation by Sakai and co-workers[25] suggest that

aggregation models, such as monomer-cluster and cluster-cluster aggregation, could be used to describe gelation at and below c*. By examining the fractal dimensions of the percolation cluster, they suggest that diffusion-limited cluster-cluster aggregation is the more likely process by which TPEG gels form.

Studies using micron sized particles to characterize gelation have also reported changes in α and N_g that could be related to changes in the network structure. Particle tracking has been used to probed heterogeneity during the gelation of colloidal suspensions of Laponite clay particles,[43] fluorenylmethoxycarbonyl-tryrosine (Fmoc-Y),[44,45] and β-glucan.[46] Donald and coworkers[45] studied Fmoc-Y gelation, which has a mesh size on the order of tens of nanometers from cryoSEM images,[44] using 0.46 μm particles. They found that N_g increased until the gel point and then remained constant. They believed this to mean that once formed, the gel had very little local heterogeneity. In the Laponite clay[43] and β-glucan[46] systems, however, N_g increased even after gelation, similar to the spike in N_g after the onset of gelation observed in this study. In the β-glucan system, which was studied using 0.75 μm carboxylate modified polystyrene particles, the N_g gradually increased prior to gelation due to differences in the local microenvironments. After gelation, N_g continued to increase due to particles becoming trapped inside pores with different sizes, which the authors suggested ranged from 1 to 15 μm. At longer times after the gel point, N_g decreased due to coarsening resulting in smaller, more homogeneous pore sizes. We believe a similar process occurs in our TPEG systems, as a peak in N_g was also observed after the gel point. Based on our results, we conclude that the evolution of the network begins with very open pores through which the NPs can move easily and diffusively. As time proceeds, the network filled in heterogeneously, resulting in disparate local environments and heterogeneity. In the final gel state, the homogeneity increases with increasing concentration, though some topological defects are to be expected.

Next, we compare our results to studies that characterize probe mobility during the sol-gel transition in TPEG gels above c* using light scattering techniques. Shibayama and coworkers[36] used an isorefractive DLS technique

to contrast match the polymer, subsequently masking the fast dynamics of polymer motion and measuring only the slow dynamics of the probe particles. The superposition of the particle mobilities can be fit using a stretched exponential function, giving the percentage of sol-fraction, $\boldsymbol{A}$, the relaxation time of the particles, $\boldsymbol{\tau}^*$, and the distribution of the particles' relaxation times, $\boldsymbol{\beta}$, as a function of reaction conversion. Similar to this work, the authors found that as the reaction conversion increased, the sol fraction decreased until the gel was completely formed. However, the distributions of the relaxation times of the probe particles, $\boldsymbol{\beta}$, does not follow the same trends as the analogous measure of heterogeneity in this study, N_g. They found that $\boldsymbol{\beta}$ monotonically decreases before the gel point, whereas in this work, N_g is relatively constant until a spike is observed near the rheological gel time. We attribute the difference in the behavior of $\boldsymbol{\beta}$ and N_g to their sensitivity to different populations of particles. In DLS, as probes become immobilized during gelation, the particles become nonfluctuating and no longer contribute to the distribution of relaxation times. Because $\boldsymbol{\tau}^*$ is only a measure of the dynamics in the sol region, $\boldsymbol{\beta}$ is expected to decrease monotonically after the gel point. N_g, however, is sensitive to both populations, namely mobile particles, as well as localized particles that become fixed in the gel. Therefore, N_g is expected to be largest at the gel point (maximum heterogeneity) because the diffusive particles experience a large range of local environments while localized particles simultaneously undergo subdiffusive motion. As gelation proceeds, more particles become immobilized and experience similar local environments (less heterogenous), and as a consequence N_g decreases. Additionally, our study uses probe particles that are on the length scale of the final mesh size (D_h = 10 nm, ζ = 3-6nm), whereas the DLS study utilizes larger particles that range from 56 nm to 114 nm. Because of this difference, dynamic heterogeneity is expected to be different between these two studies. Overall, this work complements the previous investigation by Shibayama and coworkers, and also provides new insights afforded by single particle tracking to monitor the sol-gel transition in TPEG.

Recent developments in rotational particle tracking could also be used to investigate nanoscale topological defects. Using gold nanorods, Mirsaidov and

co-workers found that even after translational diffusion had been arrested during poly(acrylamide) gelation, single nanorods were able to exhibit distinct modes of rotation, indicating heterogeneity in the local environment of the rod. Similarly, Crocker and co-workers[47] visualized the rotational diffusion of single nanorods to investigate heterogeneity in other soft matter systems. In both studies, size of the probe, ~20x100nm, is larger than the mesh of TPEG hydrogels. As methods to both synthesize smaller anisotropic particles and measure their rotational diffusion develops, studies of anisotropic probes could yield valuable information about the distribution of nanoscale topological defects in hydrogels.

4 Conclusion

In this study, SPT of 10 nm diameter NPs was used to examine the gelation of TPEG networks as polymer concentration was decreased. Interestingly, the formation of these homogenous networks was not a dynamically homogeneous process. Using rheometry, the onset of the network formation, t_{gel}, increased from less than 2 to 44 minutes as TPEG concentration decreased from 40 to 20 mg/mL. NP mobility, however, remained diffusive at times past t_{gel}, indicating that the initial network had a large mesh size relative to the size of the NPs. At longer times, NP mobility became sub-diffusive, as reflected in $\alpha < 1$ which corresponded to a peak in N_g. This dynamic heterogeneity was attributed to variations in mesh size during network formation. Eventually at long times in all concentrations, NPs became localized, which corresponded to greater dynamic homogeneity, which is consistent with a relatively homogeneous final mesh structure. The findings of this study highlight how different measurement techniques provide unique findings for the same phenomena of gel network formation due to the different length scales being probed. Rheometry measures percolation which controls mechanical characteristics of the gel structure; SPT of NPs on the size of the gel network allows for nanoscale heterogeneity to be measured. Ultimately, these results shed light on the gelation mechanism of these nearly homogeneous gels, which

will aid in their use as model systems to test polymer gel theories and in applications such as injectable drug delivery systems.

Conflicts of interest

The authors declare no competing financial interest.

Acknowledgements

Support was provided by the NSF/CBET 1706014 (RJC, EP), NSF PIRE OISE-1545884 (RJC, DL, KAR), ACS/PRF 54028-ND7 (RJC, EP), NSF Graduate Fellowship (EP, KAR), NSF/DMR 1905912 (RJC), and MRSEC/DMR 1720530 (MC, CBM, RJC). The single particle tracking experiments were performed at the Scanning and Local Probe Facility at the Singh Center for Nanotechnology at the University of Pennsylvania. The authors thank Dr. Matt Brukman for instrument support, Dr. Nadia Krook for TEM images, and Dr. Jason Burdick for the use of his rheometer.

Notes and references

1 T. Sakai, *Reactive and Functional Polymers*, 2013, **73**, 898–903.
2 T. Sakai, *Polymer Journal*, 2014, **46**, 517–523.
3 T. Sakai, T. Matsunaga, Y. Yamamoto, C. Ito, R. Yoshida, S. Suzuki, N. Sasaki, M. Shibayama and U. Chung, *Macromolecules*, 2008, **41**, 5379–5384.
4 K. Hashimoto, K. Fujii, K. Nishi, T. Sakai and M. Shibayama, *Macromolecules*, 2016, **49**, 344–352.
5 T. Matsunaga, T. Sakai, Y. Akagi, U. Chung and M. Shibayama, *Macromolecules*, 2009, **42**, 1344–1351.
6 T. Matsunaga, T. Sakai, Y. Akagi, U. Chung and M. Shibayama, *Macromolecules*, 2009, **42**, 6245–6252.
7 K. Hashimoto, K. Fujii, K. Nishi, T. Sakai, N. Yoshimoto, M. Morita and M. Shibayama, *J. Phys. Chem. B*, 2015, **119**, 4795–4801.
8 R. Shioiri, H. Kokubo, T. Horii, Y. Kobayashi, K. Hashimoto, K. Ueno and M. Watanabe, *Electrochimica Acta*, 2019, **298**, 866–873.
9 S. Ishii, H. Kokubo, K. Hashimoto, S. Imaizumi and M. Watanabe, *Macromolecules*, 2017, **50**, 2906–2915.
10 A. Ishikawa, T. Sakai and K. Fujii, *Polymer*, 2019, **166**, 38–43.
11 C. Lin, Z. Li, K. Lei, H. Jia, L. Yu, Z. Zheng and X. Wang, *Macromolecular Materials and Engineering*, 2018, **303**, 1700542.
12 D. E. Apostolides, T. Sakai and C. S. Patrickios, *Macromolecules*, 2017, **50**, 2155–2164.

13 Y. Bu, L. Zhang, G. Sun, F. Sun, J. Liu, F. Yang, P. Tang and D. Wu, *Advanced Materials*, 2019, **31**, 1901580.
14 M. S. Rehmann, K. M. Skeens, P. M. Kharkar, E. M. Ford, E. Maverakis, K. H. Lee and A. M. Kloxin, *Biomacromolecules*, 2017, **18**, 3131–3142.
15 J. Henise, B. R. Hearn, G. W. Ashley and D. V. Santi, *Bioconjugate Chem.*, 2015, **26**, 270–278.
16 Y. Zhang, N. Ding, T. Zhang, Q. Sun, B. Han and T. Yu, *Front. Chem.*, 2019, **7**, 682.
17 Y. Yoshikawa, N. Sakumichi, U. Chung and T. Sakai, *Soft Matter*, 2019, **15**, 5017–5025.
18 K. Nishi, H. Asai, K. Fujii, Y.-S. Han, T.-H. Kim, T. Sakai and M. Shibayama, *Macromolecules*, 2014, **47**, 1801–1809.
19 S. Kondo, H. Sakurai, U. Chung and T. Sakai, *Macromolecules*, 2013, **46**, 7027–7033.
20 M. Shibayama, X. Li and T. Sakai, *Ind. Eng. Chem. Res.*, 2018, **57**, 1121–1128.
21 Y. Tsuji, X. Li and M. Shibayama, *Gels*, 2018, **4**, 50.
22 Y. Akagi, T. Katashima, Y. Katsumoto, K. Fujii, T. Matsunaga, U.-I. Chung, M. Shibayama and T. Sakai, *Macromolecules*, 2011, **44**, 5817–5821.
23 F. Lange, K. Schwenke, M. Kurakazu, Y. Akagi, U. Chung, M. Lang, J.-U. Sommer, T. Sakai and K. Saalwächter, *Macromolecules*, 2011, **44**, 9666–9674.
24 M. Kurakazu, T. Katashima, M. Chijiishi, K. Nishi, Y. Akagi, T. Matsunaga, M. Shibayama, U. Chung and T. Sakai, *Macromolecules*, 2010, **43**, 3935–3940.
25 T. Sakai, T. Katashima, T. Matsushita and U. Chung, *Polym J*, 2016, **48**, 629–634.
26 T. Katashima, H. Sakurai, U. Chung and T. Sakai, *J. Soc. Rheol., Jpn*, 2019, **47**, 61–66.
27 T. H. Larsen and E. M. Furst, *Phys. Rev. Lett.*, 2008, **100**, 146001.
28 C. Veerman, K. Rajagopal, C. S. Palla, D. J. Pochan, J. P. Schneider and E. M. Furst, *Macromolecules*, 2006, **39**, 6608–6614.
29 K. M. Schultz, A. D. Baldwin, K. L. Kiick and E. M. Furst, *Macromolecules*, 2009, **42**, 5310–5316.
30 H. E. Cingil, W. H. Rombouts, J. van der Gucht, M. A. Cohen Stuart and J. Sprakel, *Biomacromolecules*, 2015, **16**, 304–310.
31 M. E. Grady, E. Parrish, M. A. Caporizzo, S. C. Seeger, R. J. Composto and D. M. Eckmann, *Soft Matter*, 2017, **13**, 1873–1880.
32 E. Parrish, M. A. Caporizzo and R. J. Composto, *J. Chem. Phys.*, 2017, **146**, 203318.
33 C. H. Lee, A. J. Crosby, T. Emrick and R. C. Hayward, *Macromolecules*, 2014, **47**, 741–749.
34 S. W. Chee, U. Anand, G. Bisht, S. F. Tan and U. Mirsaidov, *Nano Letters*, 2019, 2871–2878.
35 E. Parrish, S. C. Seeger and R. J. Composto, *Macromolecules*, 2018, **51**, 3597–3607.
36 X. Li, N. Watanabe, T. Sakai and M. Shibayama, *Macromolecules*, 2017, **50**, 2916–2922.
37 F. Ruhnow, D. Zwicker and S. Diez, *Biophysical Journal*, 2011, **100**, 2820–2828.
38 N. Tarantino, J.-Y. Tinevez, E. F. Crowell, B. Boisson, R. Henriques, M. Mhlanga, F. Agou, A. Israël and E. Laplantine, *J Cell Biol*, 2014, **204**, 231–245.
39 B. Wang, S. M. Anthony, S. C. Bae and S. Granick, *PNAS*, 2009, **106**, 15160–15164.
40 W. K. Kegel and and A. van Blaaderen, *Science*, 2000, **287**, 290–293.
41 F. Chambon and H. H. Winter, *Polymer Bulletin*, 1985, **13**, 499–503.
42 T. Sakai, Y. Akagi, T. Matsunaga, M. Kurakazu, U. Chung and M. Shibayama, *Macromolecular Rapid Communications*, 2010, **31**, 1954–1959.
43 F. K. Oppong, P. Coussot and J. R. de Bruyn, *Phys. Rev. E*, 2008, **78**, 021405.
44 A. Aufderhorst-Roberts, W. J. Frith, M. Kirkland and A. M. Donald, *Langmuir*, 2014, **30**, 4483–4492.

45 A. Aufderhorst-Roberts, W. J. Frith and A. M. Donald, *Soft Matter*, 2012, **8**, 5940–5946.
46 T. Moschakis, A. Lazaridou and C. G. Biliaderis, *Food Hydrocolloids*, 2014, **42**, 81–91.
47 M. Molaei, E. Atefi and J. C. Crocker, *Phys. Rev. Lett.*, 2018, **120**, 118002.

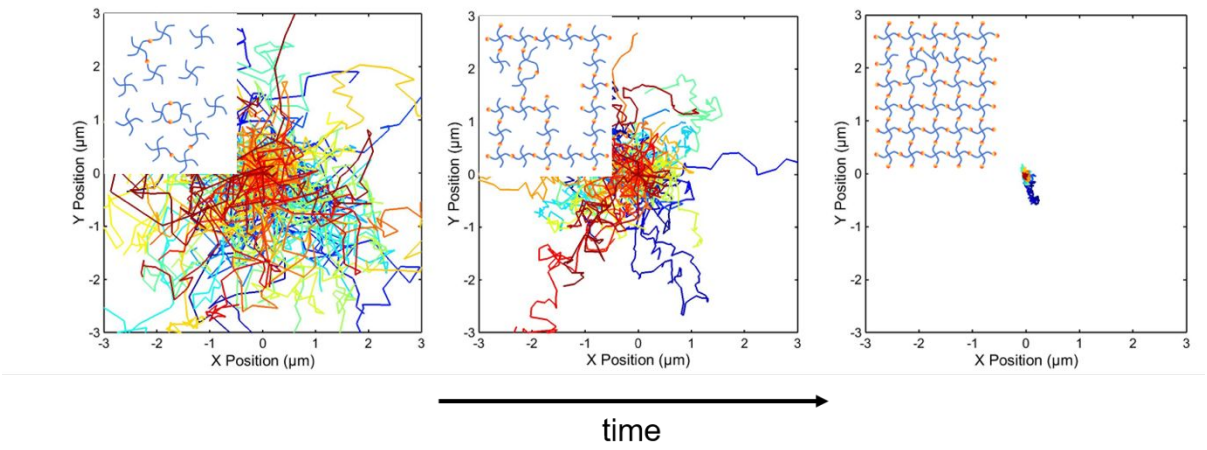

for table of contents use only.